Journal of ELECTRONIC MATERIALS, Vol. 37, No. 9, 2008
DOI: 10.1007/s11664-008-0438-z

Numerical Analysis of a Very Long-Wavelength HgCdTe Pixel Array for Infrared Detection

DANILO D'ORSOGNA,[1] STEPHEN P. TOBIN,[2] and ENRICO BELLOTTI[1,3]

1.—ECE Department, Boston University, 8 Saint Mary's Street, Boston, MA 02215, USA. 2.—BAE Systems, 2 Forbes Road, Lexington, MA 02421, USA. 3.—e-mail: bellotti@bu.edu

In this paper we present numerical simulations of pixel arrays for detection of very long-wavelength (≥14 μm) infrared radiation. The drift-diffusion equations are solved on a three-dimensional finite element grid; this approach avoids errors typically introduced by one- or two-dimensional simplifications which are difficult to quantify. We simulate the device structure and compare our numerical results with values measured on fabricated and characterized devices. The aim is to test the quality of the HgCdTe material model and derive insights for geometry optimization of pixel array detectors grown by liquid-phase epitaxy.

Key words: Infrared detectors, HgCdTe, photovoltaic detector, pixel arrays

INTRODUCTION

In 1958 the Royal Radar Establishment in England synthesized HgCdTe[1] as a result of their attempt to engineer a direct-bandgap semiconductor that could be tailored for specific applications in the long-wave IR (LWIR) spectral region (8 μm to 14 μm). Since then, HgCdTe has emerged as the standard material for IR detection in a broad range of temperatures,[2] especially in the LWIR and very long-wave IR (VLWIR) region of the spectrum (>14 μm). Among the characteristics that contributed to the success of HgCdTe are the direct energy bandgap, the possibility of having both low and high carrier concentrations, the high electron mobility, and the extremely low change in lattice constant with composition.[3] This last feature in particular has been exploited to grow high-quality HgCdTe layers for devices with improved detection performance.[4] Since its first synthesis, HgCdTe has given rise to three different generations of devices.[5–7] The first relied on linear arrays with up to 180 elements of photoconductive (PC) detectors for scanning systems generated images. The second generation consists of two-dimensional arrays of photovoltaic (PV) pixels which are scanned electronically to build the image. Among the advantages of PV detectors are better sensitivity and spectral resolution, negligible 1/*f* noise, and low or zero bias power.[8] The third generation of HgCdTe detectors are not as clearly defined as the previous cases but includes structures for enhanced detection; these can be, but are not limited to, large-format arrays, and two-color, avalanche, and quantum well detectors.

HgCdTe infrared detectors can be useful for a variety of applications but high production and development costs have limited their use to military and space applications[9]; in 2002 only 10% of the market was estimated to be commercial.[10] In such an environment, computer-aided simulations can be an extremely useful tool for the analysis of existing devices, and for the design of new optimized ones as well. In this work, we extend a previous model that we developed to study the *I–V* characteristics and photoresponse of two-color HgCdTe IR detectors.[11] The comparison of numerical results with experimental data[11] proved the effectiveness and accuracy of our model for devices made with regions of constant material properties.[12] With the present work we overcome the limitation due to uniform material and present a new model that allows for regions with graded composition profiles. The model enhancement is crucial since it will allow us to

(Received November 20, 2007; accepted February 27, 2008; published online March 27, 2008)

simulate and predict the performance of state-of-the-art HgCdTe detectors made by liquid-phase epitaxy (LPE) technology,[4] which now features compositionally graded $Hg_{1-x}Cd_xTe$ profiles. The bandgap can be engineered to optimize the collection of the photogenerated minority carriers and the result is an improved quantum efficiency with values higher than 90%. The objective of this work is to test the accuracy of the new HgCdTe material model and show that three-dimensional computer-aided simulations can be successfully used to optimize geometry and performance of these pixel arrays for PV, back-illuminated focal-plane array (FPA) detectors. The model is tested through the comparison of numerical results from full three-dimensional (3D) simulations of 3×3 pixel arrays against experimental data from BAE Systems. To the authors knowledge, this is the first time that such an approach has been pursued using a 3D replica of a HgCdTe graded-composition detector array. The use of 3D devices will avoid the typical approximations introduced by 2D pixel analysis, which are difficult to quantify. Additionally the 3×3 array will allow the calculation of crosstalk effects between the center and the surrounding pixels.

The manuscript is organized as follows: in the Section "Device Geometry and Simulation Model" we describe the device geometry, doping, and composition profiles together with the requirements for an accurate and efficient mesh grid generation. In the Section "Single-Pixel Results" we introduce the single-pixel results by comparing the numerically generated and the measured data. the Section "Crosstalk Analysis" will show the crosstalk effect between the center pixel of the detector and the neighbors. In the "Conclusions" we will summarize the conclusions of the present work.

DEVICE GEOMETRY AND SIMULATION MODEL

To ensure a reliable comparison between the simulated pixel array and the measured data we have replicated, as closely as possible, the geometry and characteristics of a typical pixel with graded composition grown at BAE Systems. In this section we introduce the single-pixel geometry together with doping and composition profiles and we will also discuss the criteria adopted in the mesh generation process.

The arrays considered in this work have a 3×3 format and the pixels have p-on-n polarity. As shown in Fig. 1, every pixel can be identified by the 24 μm $\times$ 19 μm etched mesa and its corresponding 40 μm $\times$ 35 μm cell in the bulk region. Each mesa lateral surface is represented with a 3.5-μm-radius cylindrical surface, as shown in the close-up of Fig. 2. The p-on-n device junctions are obtained from a two-layer structure where the n-type absorption layer is doped with an indium concentration of 8×10^{14} cm^{-3} and the p-type cap layer is doped with an arsenic concentration of 2.5×10^{17} cm^{-3}. The profiles used in our simulations provide an excellent fit to the measured secondary-ion mass spectroscopy (SIMS) data, as shown in Fig. 3. The arsenic concentration decay is accurately fitted by an error function and this is of primary importance since it will determine the junction depth and detector performance in general. According to our numerical results the junction dimensions are 24.76 μm $\times$ 19.76 μm and the p–n junction is located at 1.584 μm depth, in good agreement with a typical value of 1.5 μm for the real detectors.

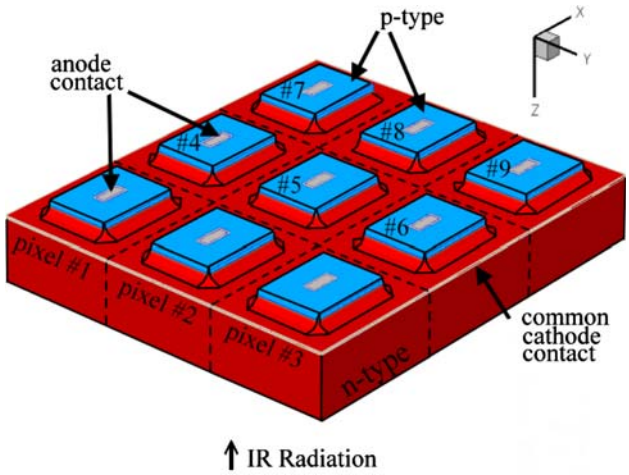

Fig. 1. Simulated pixel array with 40 μm $\times$ 35 μm cell and 24 μm $\times$ 19 μm mesa sizes. Each pixel is uniquely labeled: #5 is the center pixel in the array; #1, #3, #7, #9 are the corner pixels and #2, #4, #6, #8 are the side pixels. The cathode is chosen to be a ring at the base of the etched region.

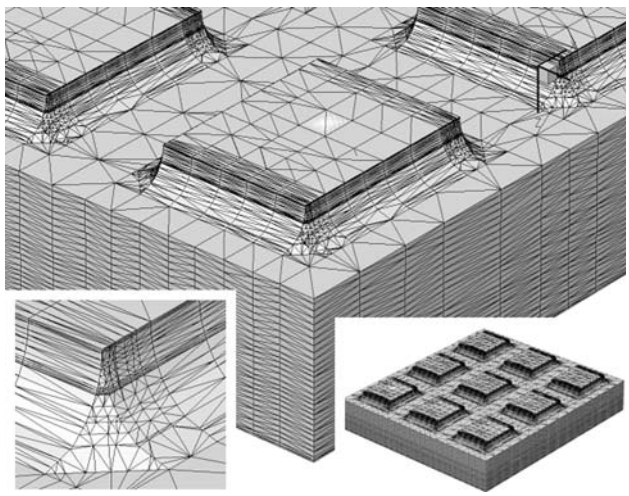

Fig. 2. Mesh grid details for the pixel array with a 40 μm $\times$ 35 μm cell and 24 μm $\times$ 19 μm mesa. The symmetry of the mesh through the entire pixel array can be appreciated. The corner view shows the mesh points falling on the separation surface between adjacent pixels, a useful feature in crosstalk simulations. From the close-up look at the mesa's corner the constant-radius surfaces used to represent the etched boundaries can be seen.

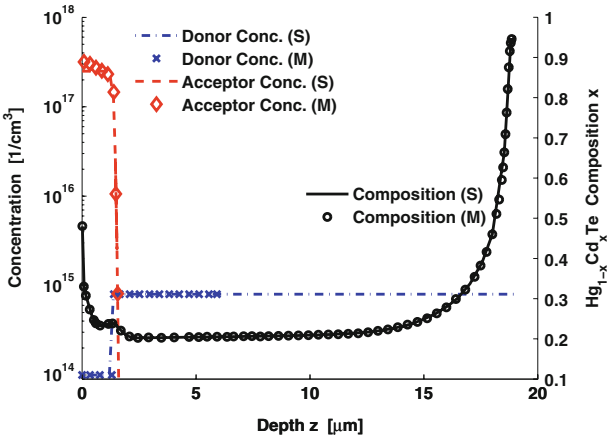

Fig. 3. Doping and composition profiles as measured (M) on a typical device at BAE Systems and the simulated (S) replica in this work. The *p*-type concentration is approximated with an error function while the *n*-type with a step function. The composition profile *x* is modeled as a piecewise-linear function in 38 steps.

The composition x will determine the photon absorption and quantum efficiency response of the detector. The measured profile from a typical detector together with the simulated one are shown in Fig. 3 on the right scale. The simulated x approximates the SIMS data through a piecewise-linear function in 38 steps chosen such that the final profile is as smooth as possible. This is particularly important since any abrupt change of slope will provide regions of accumulation of free charges in the conduction or valence band, giving rise to spikes in the electric field which will perturb the carrier dynamics. The described phenomena was clearly seen in our early attempt to approximate the variable composition with thin regions of constant x, which was then abandoned.

The incoming IR radiation is assumed to travel normally to the back-side surface of the pixel array and is first absorbed at the CdZnTe substrate interface (right of Fig. 3), where $x = 0.954$ and crosses the n-type region while the molar fraction, and therefore the bandgap, is decreasing. The lowest $x = 0.204$ together with the operating temperature T are useful for the theoretical estimation[13] of the minimum bandgap $E_{gap}(x, T)$; the cut-off wavelength can be then estimated as $\lambda_{co}(x, T) = hc/E_{gap}(x,T)$, where h is Planck's constant and c is the speed of light.

Simulated devices have ideal and light reflective contacts. Each pixel is connected to the readout integrated circuit (ROIC) chip through an 8.5 μm × 3.5 μm anode contact deposited on the 3.5-μm-high mesa center. The common cathode is 0.5 μm wide and located around the perimeter of the pixel array, at the base of the etched region (Fig. 1). For real arrays the common cathode is usually implemented by shorting the p–n junctions of the outermost array cells using metal deposited from the mesa top to the bottom of the etched region. We could certainly replicate this scenario but we would have to sacrifice a considerable number of mesh points from the maximum number available. At the time we started this work we could allocate at most 100,000 mesh points for the calculations and the trade off is therefore between the device volume to be meshed and the point density. While an exact replica of the realistic case is always desirable, we opted for the simple cathode ring shown in Fig. 1 in order to save points and obtain a tighter mesh near the p–n junctions to capture the phenomena occurring in those regions better.

In a typical electronic device the mesh density increases around the junctions to capture the occurring physical phenomena better. This approach certainly applies to the detector array case, although we add some extra considerations for our purposes. The Z direction (Fig. 1) implements the composition profile variation, which is critical for photon absorption, and we have reserved a denser mesh, as opposite to the X and Y directions (Fig. 2). In the X–Y plane our main concern was to replicate the same mesh over different pixels and make sure that pixels placed in a symmetric position with respect of the center one exhibit the same results. As an example, pixels #2 and #8 of the detector must exhibit the same behavior when equally biased and illuminated since they both share the 35 μm side of the center pixel. The same is true for pixels #4 and #6. Again for symmetry considerations, the detector array is designed such that each pixel is a shifted replica of the central one. This approach will guarantee that during the mesh generation process each pixel will be ideally bounded by planar surfaces and clearly identifiable in the bulk. This is particulary important in simulations where only the center pixel has to be illuminated, a typical set up for crosstalk current evaluation.

Once the geometry is fully specified and an optimized mesh obtained, the next necessary ingredient is the material model. For this work we employ the same composition- and temperature-dependent models we used in a previous work.[11] All the necessary optical parameters and transport coefficients have been determined from first principles without introducing any fitting procedures.

The numerical simulation is based on the drift-diffusion approach, where the coupled Poisson's and electron/hole continuity equations are solved on the finite element mesh previously described. The equations are solved using Sentaurus Device, a multidimensional device simulator from the Synopsys TCAD software package. The use of a simple drift-diffusion model is justified in this case since the detector pixels work close to, or not far from, zero bias.

Because of the large device dimensions of the 3 × 3 array, high-performance scalar and parallel linear systems solvers are used. The typical simulation will require the solution of linear systems with sparse matrix of the order of 10^5 unknowns per

physical quantity, since the examples presented in this work have meshes with 10^5 nodes.

SINGLE-PIXEL RESULTS

In this section we introduce the pixel array simulation results and verify that the design specifications are still valid after the meshing generation process.

The mesh generation process essentially introduces a discretization in the device geometry and can lead to unpredictable results in regions where physical properties are rapidly changing. To verify that the design specifications are not altered, a simulation with zero bias and in dark condition is performed for the extraction of the main parameters. In the Section "Device Geometry and Simulation Model" we have already shown and discussed the doping and composition profiles (Fig. 3). In this section we turn our attention to the band structure and electric field, both shown in Fig. 4 for a cut along the perpendicular direction (Z in Fig. 1) through the center of pixel #5. As expected for a graded material[14] the n-type region has a flat conduction band and the valence band takes into account the bandgap variation caused by the increasing molar fraction. The corresponding absolute value of the electric field is also shown in Fig. 4; it will provide a drift component for the photogenerated holes in the n-type region. In particular it will assist the hole motion toward the strong junction field, computed as 2×10^3 V/cm, which will give rise to the photovoltaic effect. In the p-type region the situation is opposite; the valence band is flat while the conduction band adjusts accordingly to the varying bandgap. In Fig. 4 it can also be noticed how the bandgap widens again at the surface, mainly to limit the leakage current at the interface with the CdTe passivation layer (not included in our simulations).

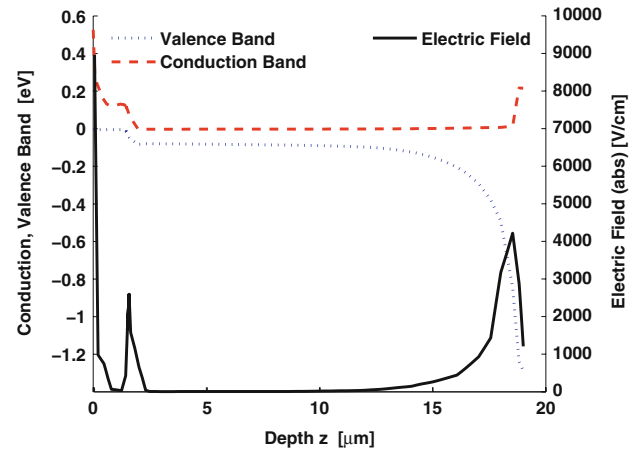

Fig. 4. Computed electric field, valence and conduction bands for a cut along the Z direction through the center of pixel #5 when all contacts are grounded (T = 51 K).

To validate our work it is essential to compare the numerical results with the measured data. We will compare our pixel #5 results with pixels of the same geometry that have been fully characterized by BAE Systems. The comparison involves basic physical quantities such as quantum efficiency, current–voltage (I–V) characteristics, and dynamic resistance R_o calculations.

Figure 5 presents the measured quantum efficiency from a backside-illuminated detector together with the response from center pixel #5 of the simulated array; the arrays are fully illuminated with grounded contacts in both measured and simulated cases. Notice also that, for this figure, and for the following in this work, no fitting parameters have been used to describe the material properties in order to fit the experimental data. The solid line represents the measured external quantum efficiency while the dot-dashed line is the calculated internal quantum efficiency. We multiply the latter by the measured transmittance of the antireflection coating on the backside of the detector (not included in our simulations) to obtain the equivalent external quantum efficiency. It is possible to notice from Fig. 5 that, although there are some discrepancies, the measured and theoretical peak values for the quantum efficiency are in good agreement. Near the cutoff wavelength the calculated quantum efficiency underestimates the measured values while the opposite is true for wavelengths slightly beyond the cutoff. This type of behavior has already been observed in simulated HgCdTe detectors and is mainly due to the model employed for the absorption coefficient. In our current simulations we use the Hougen[15] model, which provides the results shown. We are aware of recent

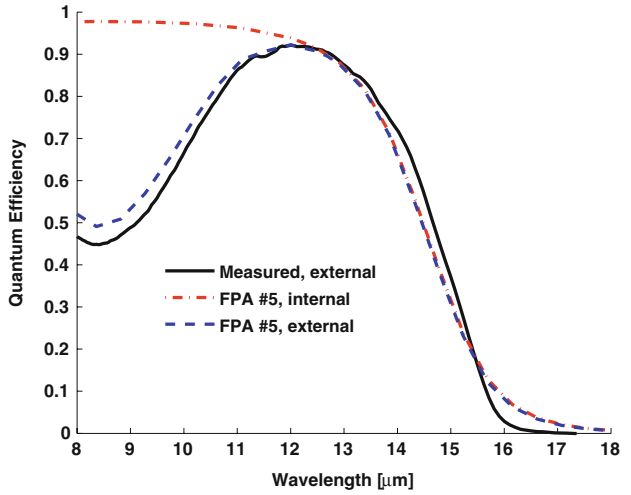

Fig. 5. Simulated and measured, internal and external quantum efficiency at 51 K with zero bias when the array is fully illuminated. The simulated internal quantum efficiency has been scaled with the transmittance of the antireflection coating to allow comparison with the measured data.

suggested improvements[16,17] and we will test them in future developments of this work. Below 11 μm the discrepancy increases; in particular the measured external data falls lower than the simulated external data, but this is mainly a measurement artifact of the experimental set-up.

To test the *I–V* characteristic of the array in dark conditions we simulated the device with a bias range of ±0.1 V in two different bias conditions. In the first case the voltage is applied only to pixel #5 while the neighbors are kept at ground level with the cathode; in the other case each anode is connected to an independent voltage source and their bias swept simultaneously. In Fig. 6 the calculated *I–V* characteristic of pixel #5 (dashed line) is compared to the measured data (solid line) when the neighboring pixels are grounded; the figure also shows for comparison the simulated characteristic of pixel #5 when the neighbor pixels have the same bias (dot-dashed line). Considering that there are no fitting parameters, the agreement between the simulated and measured data is good except for high bias voltages. The simulated current in reverse bias underestimates the measured one by a factor of 2. Some of this discrepancy is explained by the slightly longer cutoff wavelength of the measured detector relative to the modeled one (see Fig. 5). In forward bias, the difference between measurement and simulation increases at higher voltages where the series resistance of the real detector plays a major role. Although our simulations employ ideal contacts we have calculated the equivalent current with a hypothetical resistance of 300 Ω in series with the pixel anode contact. The result is shown in Fig. 6 (circles) and the calculated current shows a much better agreement with the measured one.

When the center pixel bias is swept and the neighbor contacts are grounded, the surrounding pixels will exhibit a small current. The inset in Fig. 7 shows an equivalent circuit where the diodes are interconnected through a network of equivalent resistors representing the common bulk region. The inset shows the center pixel #5, side pixel #2, and corner pixel #1 while other pixels have been neglected for simplicity.

When the anode of pixel #5 is forward biased and the neighboring pixels' anodes are grounded (Van. #2,1), the bulk region corresponding to center pixel (Vb. #5) is at a potential higher than ground. As a consequence, the bulk of the neighbor pixels (Vb. #1,2) also have a positive bias and therefore diodes #1 and #2 are reverse biased. The anode current of pixel #5 is balanced by the sum of the currents from the cathode and the neighboring pixels. The same type of current balancing, but with inverted signs, occur when the center pixel is reverse biased. Figure 7 shows the *I–V* characteristic of pixel #5 together with the absolute current value for the side pixel #2 and corner pixel #1, smaller by a factor of 6 and 40, respectively. Notice that, as explained above, pixels #2 and #1 have a current of opposite sign while the figure shows only the absolute values.

In Fig. 8 we have translated the dark *I–V* characteristics previously discussed into resistance-voltage plots. At zero bias the simulated curves differ by a factor of 6.2, depending on the bias of the neighboring pixels; the maximum difference is recorded for −0.03 V, where the separation is a factor of 10. In the case of grounded neighboring contacts the simulated and measured data are in very good agreement between −0.02 and +0.04 V. At a larger positive bias on pixel #5, series resistance causes the two curves to diverge; at lower negative bias, the experimental data approaches the limit of the test equipment.

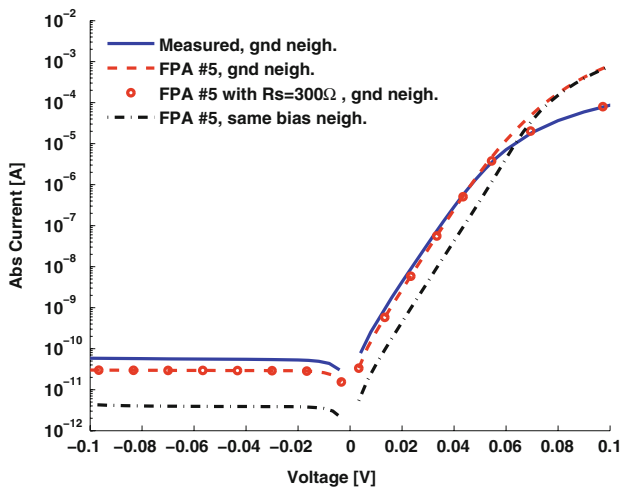

Fig. 6. Comparison for the *I–V* characteristic between measured and simulated (pixel #5). The simulated data is shown with two different bias conditions: simultaneous sweep of all contacts (dot–dashed line), grounded neighbor contacts (dashed line) (T = 51 K).

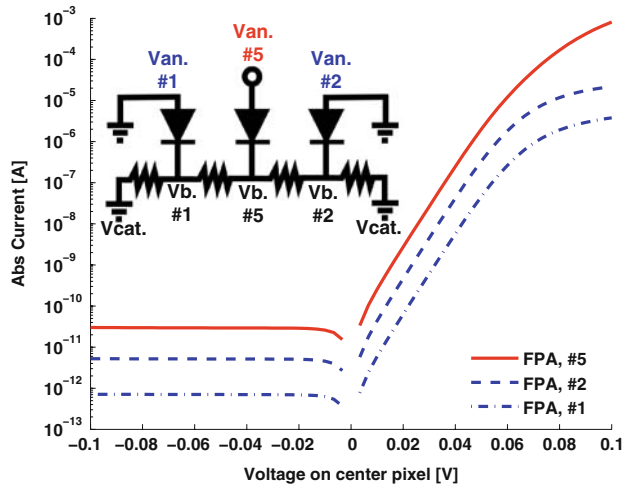

Fig. 7. Center pixel (#5) *I–V* characteristic with grounded neighbor contacts and no illumination, T = 51 K. Although the neighbor pixels have their anode contacts grounded, they will be slightly forward (reverse) biased when the center pixel is reverse (forward) biased through the common bulk.

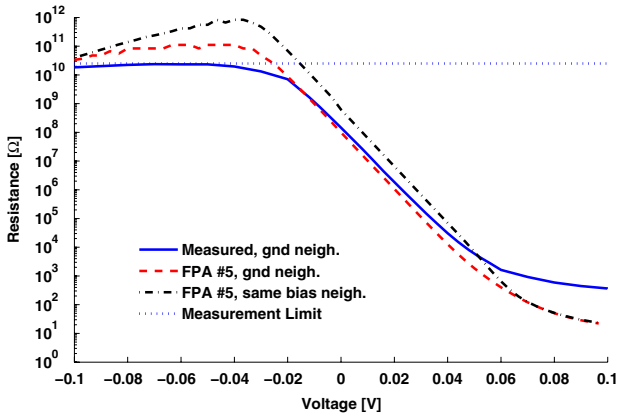

Fig. 8. Resistance calculations in dark conditions at 51 K. For zero bias there is a factor of 6.2 difference depending on the bias level of the pixels surrounding the center one (#5).

CROSSTALK ANALYSIS

In the current section we analyze the crosstalk effect for the simulated 3×3 detector array. The center pixel is illuminated with a photon flux of 1×10^{17} photons/cm^2/s and the calculated quantum efficiency is shown in Fig. 9 (dashed line); in the same figure we also show the quantum efficiency obtained for the full illumination case (solid line) as a reference for visual comparison. In the current case, the electron–hole pairs generated optically in pixel #5 are free to cross the lateral boundaries and can be collected by any of the surrounding pixels. This phenomena can also be characterized by the amount of current in the neighboring pixel contacts and provides evidence of crosstalk interaction. Figure 9 also includes the hypothetical quantum efficiency derived from this interaction, although these pixels are not directly illuminated. The dashed-dotted line represents the sum of the quantum efficiencies collected on the side pixels (#2, #4, #6, and #8), while the dotted line is the sum for the corner pixels (#1, #3, #7, and #9). The crosstalk on corner pixels is significantly lower since they do not directly share any boundary with pixel #5. The crosstalk can also be visualized with the help of Fig. 10 through the hole current density. The figure clearly shows the hole current density on the side pixels both in the top surface of the detector (3D view) and in the cross section (2D) cut along the center of pixel #5 for a wavelength of 10 μm.

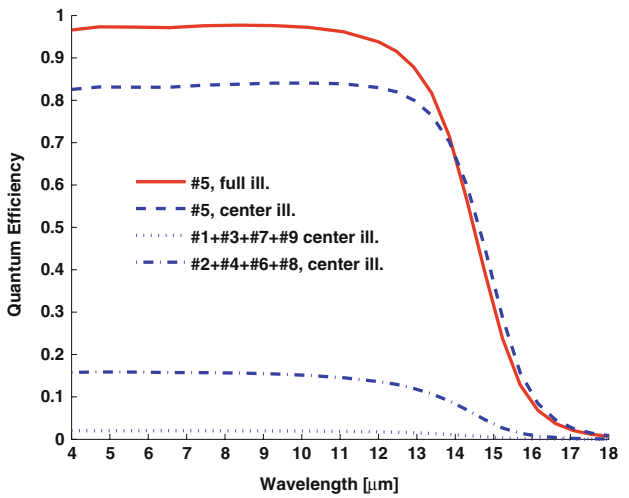

Fig. 9. Center pixel quantum efficiency calculated when the detector is fully illuminated (solid line) and illuminated only under the center pixel (dashed line); all contacts are grounded, $T = 51$ K. The quantum efficiency for side (#2, #4, #6, #8) and corner (#1, #3, #7, #9) pixels are also derived, although they are not directly illuminated.

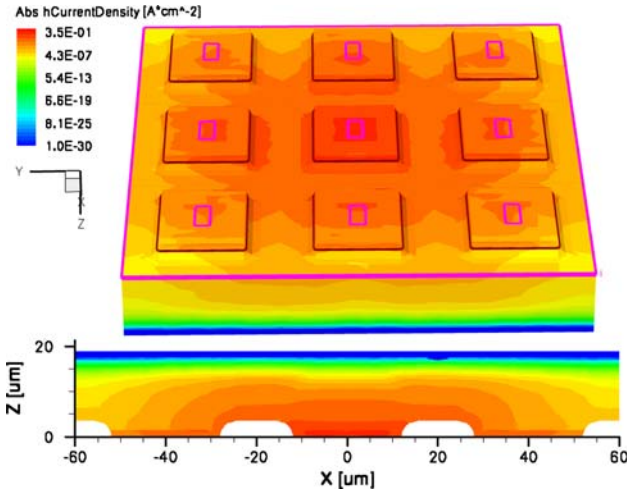

Fig. 10. Three-dimensional view of the pixel array that highlights the crosstalk between the center and corner pixels. The hole current density is shown when the center pixel is back-illuminated at a wavelength of 10 μm and $T = 51$ K. The 2D view is a cut in the X–Z plane through the center of the device.

CONCLUSIONS

In this work we have introduced full 3D simulations of multipixel detectors, based on a material model developed for HgCdTe detectors with variable composition profile. We have successfully replicated the geometry and doping profiles of pixels characterized at BAE Systems and we have analyzed their performance on 3×3 detector arrays. The numerically calculated I–V characteristics and quantum efficiency from the center pixel of the pixel array provided very good agreement with the measured data. The multipixel analysis also provided an estimation of the crosstalk effects between the center pixel of the array and the surrounding ones.

The authors believe that the developed HgCdTe model together with the full 3D approach can provide a useful and reliable tool for the analysis of current detectors and the design of new improved ones.

ACKNOWLEDGEMENTS

The authors would like to thank Dr. P. Lamarre (Photronix Inc.) and Dr. P. Lo Vecchio (BAE Systems) for supporting this work.

REFERENCES

1. W.D. Lawson, S. Nielsen, E.H. Putley, and A.S. Young, *J. Phys. Chem. Solids* 9, 325 (1959).
2. P. Norton, *Opt. Eng.* 30, 1649 (1992).
3. J. Rutkowski, *Opto-Electron. Rev.* 12, 123 (2004).
4. P. LoVecchio, K. Wong, T. Parodos, S.P. Tobin, M.A. Hutchins, and P.W. Norton, in *Proceedings of the SPIE—The International Society for Optical Engineering, Infrared Systems and Photoelectronic Technology*, vol. 5564 (2004).
5. A. Rogalski and K. Chrzanowski, *Opto-Electron. Rev.* 10, 159 (2002).
6. A. Rogalski, *Opt. Eng.* 42, 3498 (2003).
7. P. Norton, *Opto-Electron. Rev.* 14, 1 (2006).
8. M. Reine, in *Proceedings of the SPIE—The International Society for Optical Engineering, Photodetectors Material and Devices VI*, vol. 4288 (San Jose, CA, 2001).
9. P. Tribolet, *Compd. Semicond.* (2007).
10. A. Rogalsky and K. Chrzanowski, *Opto-Electron. Rev.* 10, 111 (2002).
11. E. Bellotti and D. D'Orsogna, *IEEE J. Quantum Electron.* 42, 418 (2006).
12. M. Reine, A. Hairston, P. O'Dette, S. Tobin, F. Smith, B. Musicant, P. Mitra, and F. Case, in *Proceedings of the SPIE—The International Society for Optical Engineering, Infrared Detectors and Focal Plane Arrays V*, vol. 3379 (Orlando, FL, 1998).
13. D. Seiler, J. Lowney, C. Litter, and M. LoLoee, *J. Vac. Sci. Technol. A* 8, 1237 (1990).
14. G. Margaritondo and P. Perfetti, in *Heterojunction Band Discontimuities*, ed. F. Capasso and G. Margaritondo (North-Holland, New York, 1987), pp. 59–114.
15. Hougen C.A., *J. Appl. Phys.* 66, 3763 (1989).
16. K. Moazzami, J. Phillips, D. Lee, S. Krishnamurthy, G. Benoit, Y. Fink, and T. Tiwald, *J. Electron. Mater.* 34, 773 (2005).
17. C.L. Littler, B.P. Gorman, D.F. Weirauch, P.K. Liao, and H.F. Schaake, *J. Electron. Mater.* 34, 768 (2005).